AGU PUBLICATIONS

Geophysical Research Letters

RESEARCH LETTER
10.1002/2015GL065366

Special Section:
First Results from the MAVEN Mission to Mars

First results of the MAVEN magnetic field investigation

J. E. P. Connerney[1], J. R. Espley[1], G. A. DiBraccio[1], J. R. Gruesbeck[1,2], R. J. Oliversen[1], D. L. Mitchell[3], J. Halekas[4], C. Mazelle[5,6], D. Brain[7], and B. M. Jakosky[7]

[1]NASA Goddard Space Flight Center, Greenbelt, Maryland, USA, [2]Department of Astronomy, University of Maryland, College Park, Maryland, USA, [3]Space Sciences Laboratory, University of California, Berkeley, California, USA, [4]Department of Physics and Astronomy, University of Iowa, Iowa City, Iowa, USA, [5]CNRS, IRAP, Toulouse, France, [6]IRAP, Paul Sabatier University, Toulouse, France, [7]Laboratory for Atmospheric and Space Physics, University of Colorado Boulder, Boulder, Colorado, USA

Abstract Two Mars Atmosphere and Volatile EvolutioN magnetic field sensors sample the ambient magnetic field at the outer edge of each solar array. We characterized relatively minor spacecraft-generated magnetic fields using in-flight subsystem tests and spacecraft maneuvers. Dynamic spacecraft fields associated with the power subsystem (≤1 nT) are compensated for using spacecraft engineering telemetry to identify active solar array circuits and monitor their electrical current production. Static spacecraft magnetic fields are monitored using spacecraft roll maneuvers. Accuracy of measurement of the environmental magnetic field is demonstrated by comparison with field directions deduced from the symmetry properties of the electron distribution function measured by the Solar Wind Electron Analyzer. We map the bow shock, magnetic pileup boundary, the $\mathbf{V}\times\mathbf{B}$ convection electric field and ubiquitous proton cyclotron, and 1 Hz waves in the ion foreshock region.

Key Points:
- We observe, analyze, model, and mitigate spacecraft-generated magnetic fields
- Measured field vectors are independently validated using electron analyzer observations
- We map the Mars magnetosphere, convection electric field, foreshock waves, and magnetotail

Correspondence to:
J. E. P. Connerney,
jack.connerney@nasa.gov

Citation:
Connerney, J. E. P., J. R. Espley, G. A. DiBraccio, J. R. Gruesbeck, R. J. Oliversen, D. L. Mitchell, J. Halekas, C. Mazelle, D. Brain, and B. M. Jakosky (2015), First results of the MAVEN magnetic field investigation, *Geophys. Res. Lett.*, *42*, doi:10.1002/2015GL065366.

Received 13 JUL 2015
Accepted 18 AUG 2015

1. Introduction

The Mars Atmosphere and Volatile EvolutioN (MAVEN) mission seeks to understand the history of climate change on Mars by studying the present state of the Mars upper atmosphere and ionosphere and the processes governing atmospheric loss to space [*Jakosky et al.*, 2015a]. The MAVEN science payload includes a suite of instruments ("Particles and Fields Package") designed to work together to characterize the plasma environment of Mars and its interaction with the solar wind. The magnetometer (MAG) measures the vector magnetic field at 32 samples/s [*Connerney et al.*, 2015] and provides the rest of the instrument suite (see *Jakosky et al.*, 2015a) with field vectors in real time to optimize pitch angle sorting and binning of data before transmission to the ground.

Accurate knowledge of the magnetic field magnitude and direction is a prerequisite for interpretation of the particle observations and critical to the understanding of ion pickup and flow (and escape). It is particularly important to have an accurate determination of the vector field in the weak field environments of the solar wind and distant magnetotail. This is often the most challenging measurement requirement for a magnetic field investigation due to the potential for magnetic interference from the spacecraft itself. This problem is often addressed by the imposition of a strict magnetic control program in the design, construction, and testing of the spacecraft [*Jakosky et al.*, 2015a; *Connerney et al.*, 2015] and by in-flight characterization of the spacecraft field [e.g., *Acuña et al.*, 2001]. The MAVEN spacecraft magnetic field was not to exceed 2 nT static and 0.25 nT variable, measured at the magnetometer sensor locations. The static field can be measured in-flight (using occasional spacecraft maneuvers) and analytically removed from observations.

The space environment is very difficult, if not impossible, to faithfully replicate in the laboratory, and oftentimes flight experience provides the best assessment of spacecraft magnetic cleanliness.

In this report we describe the in-flight characterization of the MAVEN spacecraft magnetic field and describe the model used to analytically correct the observations. We present an analysis of the angular distribution of solar wind electrons to independently verify the accuracy of magnetic field vectors provided by the magnetic field investigation, particularly in weak field environments where the effects of spacecraft-generated magnetic fields are most visible. The first few months of MAVEN magnetic field observations are used here to map the interaction regions of the Mars magnetosphere, quantify the $\mathbf{V}\times\mathbf{B}$ convection electric field

Table 1. Estimates of Combined Spacecraft/Sensor Offsets (+*Y* Sensor, nT)

Event	Year - DOY	Environment	O_x	O_y	O_z	Comments
1	2014 - 311	Solar wind	−0.388	−2.125	−0.743	Few rotations used; environmental noise
2	2014 - 353	Solar wind	−0.376	−1.950	−1.010	Environmentally benign; entire sequence used
3	2015 - 115	Magnetotail	−0.204	−2.178	−0.945	Environmentally benign; ~10 nT ambient
4	2015 - 116	Magnetotail	−0.045	−1.939	−0.741	Relatively disturbed conditions; ~8 nT ambient
5	2015: 115/116	Magnetotail	−0.147	−2.057	−0.945	Combined set 115/116 for robust estimate

that is so important to loss processes, and describe foreshock wave activity (relevant to ion pickup and atmospheric escape) and the dynamical behavior of the induced magnetotail.

2. Spacecraft Magnetic Control and Mitigation

2.1. Static Spacecraft Magnetic Field

The magnetometer sensors are accommodated at the very end of the solar array panels on modest extensions (2/3 m length) called MAG "boomlets". They are ~5.6 m from the center of the spacecraft, minimizing spacecraft-generated magnetic fields, by virtue of the $1/r^3$ diminution of a magnetic (dipole) source with distance. The primary magnetometer sensor resides on the outermost panel of the +*Y* array and the secondary sensor resides on the –*Y* array (see Figure 21 of *Connerney et al.,* 2015).

Static or relatively constant spacecraft magnetic fields are estimated by performing spacecraft roll maneuvers every few months during the mission. These maneuvers provide a set of rotations about two orthogonal axes. The maneuvers, and the method of analysis applied to them, are described in detail elsewhere [*Connerney et al.*, 2015]. We executed four MAGROLL maneuvers subsequent to deployment of the articulated payload platform. The maneuver consists of 10 spacecraft rotations about an axis close to the spacecraft *z* axis ("*z* axis rolls"), followed by another 10 about an axis near the spacecraft *x* axis ("*x* axis rolls"). A set of 10 rotations requires ~40 min. The *z* and *x* axes rolls are scheduled to execute on sequential orbits, to avoid spilling over into regions (e.g., magnetosheath) characterized by excessive variations in field magnitude and direction. The solar arrays are effectively turned off during the maneuver, via a command to reduce the state of charge (SOC) of the batteries, eliminating the possibility of introducing a time-varying magnetic signal related to illumination.

Two MAGROLLs, on days of year (DOY) 311 and 353, 2014, were scheduled to occur when MAVEN was in the weak (and quiet) solar wind and beyond the reach of strong crustal fields [*Connerney et al.*, 2005]: the other two while MAVEN traversed the distant magnetotail where favorable conditions were expected. These occurred on DOY 115 and 116, 2015, notably while the spacecraft was in darkness, shadowed by Mars.

Table 1 lists the static field offsets ($O_{x,y,z}$) deduced from MAGROLL maneuvers. Events 2, 3, and 5 are considered the most robust as they were acquired during relatively benign (quiet and steady) conditions. Using these estimates, assuming the spacecraft field has remained constant, the average static field is $[-0.242 \pm 0.134,\ -2.061 \pm 0.110,\ -0.966 \pm 0.04]$ in (+*Y*) sensor coordinates. The "static" spacecraft field is indeed reasonably constant, and MAGROLL maneuvers performed under suitable conditions are sufficient to estimate the field with a repeatability of ~0.15 nT or so.

2.2. Dynamic Spacecraft Magnetic Field

With a pair of magnetic sensors on opposite ends of the spacecraft, we monitor spacecraft-generated magnetic fields by forming the difference between the two measurements in spacecraft payload coordinates. We identified spacecraft-generated magnetic fields associated with thruster operation (used infrequently for orbital trim maneuvers), reaction wheels, and the power subsystem (solar array circuits). Thruster operation produces a distinctive and easily recognizable signal [*Connerney et al.*, 2015] during the burn, attributed to the momentary energization of solenoids controlling fuel flow. Magnetic fields associated with four reaction wheel assemblies (RWAs) appear at the (variable) frequency of operation of the individual wheels when within the passband (0–16 Hz) of the magnetometers. The amplitude of the periodic RWA signal is typically quite low (0.1–0.2 nT) but sometimes increases at very low RWA speeds (<0.1 Hz), which is discussed in an example later.

We observed variations in the magnetic field associated with solar array operation, due to switching of circuits on the outer solar array panels. During cruise we detected step variations in the field at the –*Y* sensor location (~1 nT) and the +*Y* sensor location (~0.5 nT) when the solar arrays were switched off via a command to reduce the state of charge (SOC) of the batteries. In-flight testing demonstrated that the magnitude of the field attributed to the outermost solar array circuits scaled linearly with illumination angle and thus the magnitude of current flowing in the illuminated circuits. In this test the spacecraft was commanded to various insolation angles (0°, ±35°, ±70° relative to spacecraft *z* axis), and the arrays were toggled off and on via the SOC command.

Once this test confirmed the source of the magnetic interference, we designed a more comprehensive test to characterize the magnetic field produced by each individual circuit on the outer solar array panel. Solar array circuits are switched on and off dynamically by the solar array switching module (SASM). It is possible to disable the autonomous operation of the SASM and operate it manually, to address individual circuits among the many that operate at any time. This is routinely done before launch but never before in-flight. We used this facility to disable all SASM circuits but for one under test. The solar array circuit under test was fully illuminated, and commands to the SASM were used to switch the circuit under test on and off using a recognizable pattern. We exercised every circuit on both of the outer solar array panels in this manner, one after the other, to obtain a relationship between the circuit switch state (on or off and current conducted) and the magnetic field produced at both sensor locations. We found that five of the outermost six circuits (three on each side) contributed a non-negligible magnetic field when illuminated.

The field produced by each of these circuits is directed along the outer panel normal, consistent with incomplete cancelation of the solar cell strings via the "backwire" loop on the underside of the panel. Circuits 8, 10, and 12 on the +*Y* panel contribute 0.175, 0.0, and 0.116 nT/A when illuminated and switched "on"; circuits 28, 30, and 32 on the –*Y* panel contribute 0.161, 0.093, and 0.259 nT/A. Each circuit conducts ~2 amperes when fully illuminated in orbit about Mars.

We now acquire measurements of the switch states and current conducted in these circuits at the highest sample rate available (2.5 Hz). We use this knowledge to compute the field at each sensor location produced by these five circuits as a function of time. The measured magnetic field is corrected for this dynamic spacecraft field in processing level 2 archive data. Observations obtained prior to the routine availability of high rate engineering (DOY 9, 2015) are corrected but with less fidelity in time, subject to the less frequent updates available from spacecraft engineering telemetry.

3. Comparison With Electron Analyzer Observations

With the comprehensive particle instrumentation on MAVEN, we can provide an independent and ongoing assessment of the accuracy of the magnetic field vectors produced by MAG. This is particularly useful in weak fields where uncompensated spacecraft magnetic interference would bias vector field directions. We do this by comparison of the magnetic vector with observations of the electron distribution function. The electron strahl distribution is particularly useful for this; the strahl is a population of solar wind electrons (energies $>$ 80 eV) that propagate in beams parallel to the magnetic field direction [*Feldman et al.*, 1975; *Rosenbauer et al.*, 1977]. The Solar Wind Electron Analyzer (SWEA) (D. L. Mitchell et al., The Solar Wind Electron Analyzer, submitted to *Space Science Reviews*, 2015) on MAVEN measures electrons with energies from 5 eV to 4.6 keV with a field of view of 360° by 120°. This instrument is used to compute the three-dimensional distribution of the observed electron flux, over 4 s intervals, from which we obtain the unit vector direction along which the strahl electrons propagate. When the magnetic field is relatively weak, and steady, these strahl directions can be compared to the corresponding MAG vectors. To overcome the limited (22.5°) angular resolution of the SWEA instrument, we analyze an ensemble of events that span adjacent angular bins (i.e., "dithering" to improve resolution). We combine many such observations in a statistical sense to assess how well, on average, the MAG vector agrees with the electron symmetry angle from SWEA.

Figure 1 shows MAG and SWEA measurements acquired on 11 November 2014. From Figures 1a–1d we show the magnitude and three components of the magnetic field, followed by electron distribution symmetry angles. Highlighted in blue is a period of time (8:02:40 to 9:03:48) during which the magnetic field was

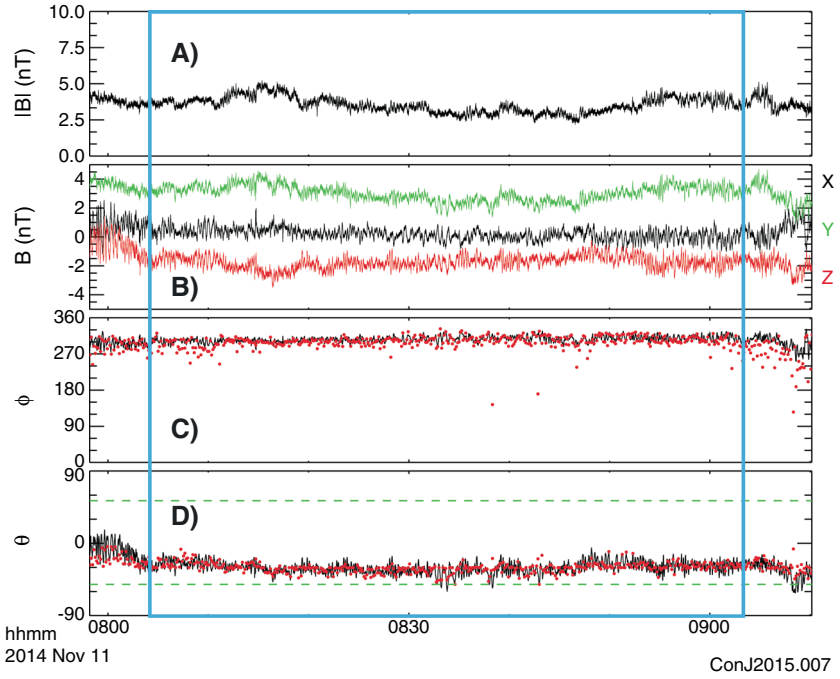

Figure 1. Plot of the (a) magnetic field magnitude, (b) *x*, *y*, *z* components in black, green, and red and (c) SWEA electron symmetry azimuth and (d) elevation angles (red symbols) in spacecraft payload coordinates, on 11 November 2014. MAG vector azimuth and elevation angles (black line) are shown in Figures 1c and 1d for comparison. The analysis interval is indicated (blue box).

relatively weak ($<$5 nT), and the direction of the field varies slowly. Thus, the SWEA instrument, at 4 s cadence, can provide estimates of the magnetic field direction to be compared with MAG observations.

MAG observations are averaged over SWEA's 4 s observation interval for comparison with the electron symmetry angle. The symmetry angle provides an estimate of the (unit vector) direction of the field, subject to a 180° ambiguity. So we scale SWEA unit vectors with the measured magnetic field magnitude and sense to obtain vectors of the same length in units of nT. The vector components of the measured magnetic field are subtracted from the SWEA vector components to determine the vector offset between the two. In Figures 2a–2c we show histograms of the vector difference observed during four quiet periods in November 2014. This set of observations includes vector directions fitted to 1197 individual SWEA electron distributions (4 s each). The median difference between the *x*, *y*, and *z* components of the MAG and SWEA vectors are -0.137 nT, -0.019 nT, and 0.019 nT, respectively. For these weak field intervals, MAG and SWEA vectors are indeed remarkably consistent. In Figure 2d we show a three-dimensional representation of the median direction of the MAG vector (red) and SWEA vector (blue) as well as dots on the unit sphere for individual measurements. The two vectors are nearly aligned, and the angular distributions of MAG and SWEA vectors are similar.

As of this date, we have compared MAG level 2 archive data and SWEA measurements for 27 periods during November 2014 and January–March 2015. We find a compelling agreement between the MAG and SWEA measurements (Figure 2) when the magnetic field direction is slowly varying. This comparison provides an independent verification of the accuracy of MAG vector directions indicating that compensation for spacecraft fields has been very effective.

4. Initial Science Results

4.1. Magnetospheric Configuration, Magnetic Fluctuations, and Convection Electric Field

The magnetic field is a critical quantity for organizing charged particle measurements, both for analysis of individual distribution functions and for organizing measurements of particles traveling through the

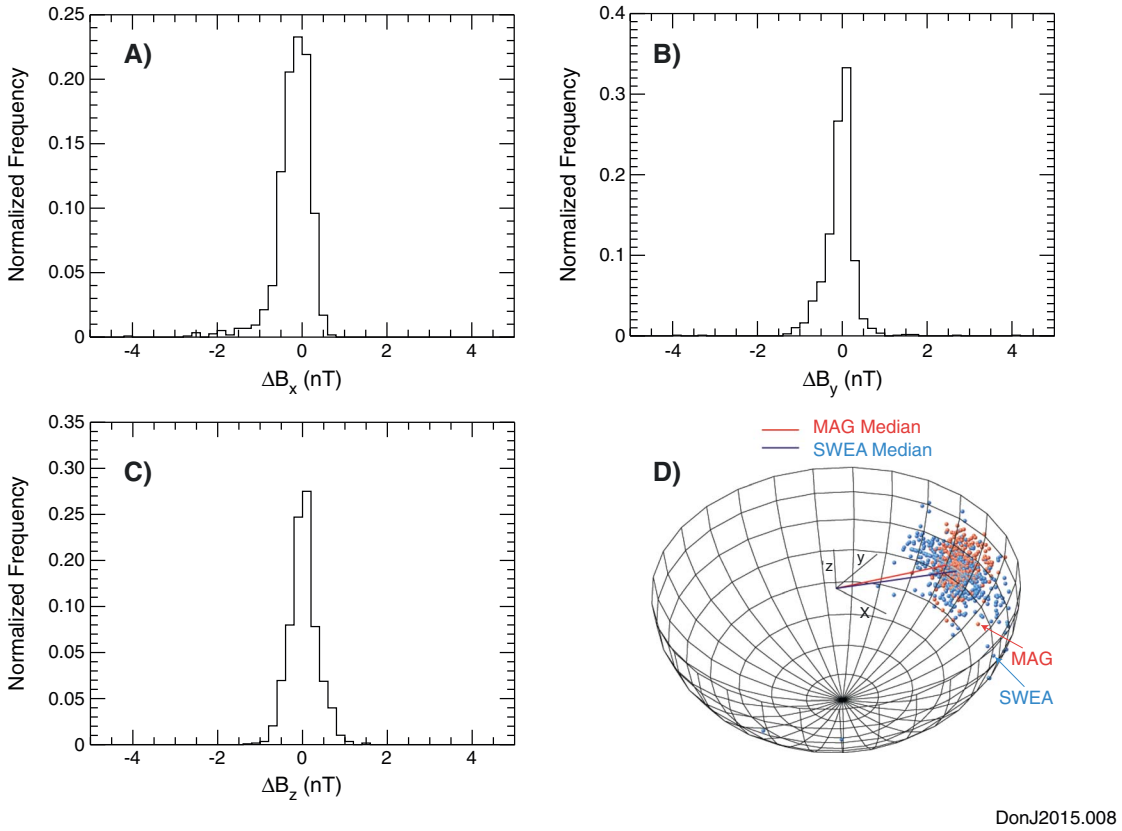

Figure 2. Comparison of MAG observations and SWEA electron symmetry angles for selected time intervals in November 2014. (a–c) Histograms of the *x*, *y*, and *z* components, respectively, of the MAG and SWEA offset vectors (in nT) for each SWEA measurement. (d) A scatter plot of MAG (red dots) and SWEA (blue dots) vector directions and the mean MAG (red) and SWEA (blue) vector directions for a typical analysis interval (shown in Figure 1).

magnetosphere and escaping into interplanetary space [*Brain et al.*, 2015]. The inclusion of a magnetometer along with a comprehensive suite of charged particle instruments provides one of the key capabilities that distinguish MAVEN from previous missions. Figure 3 compiles measurements from the MAVEN magnetometer, demonstrating the power of MAG observations for organizing the structure of the Martian magnetosphere. The magnetic field shows the expected draping pattern [*Crider et al.*, 2004; *Bertucci et al.*, 2003], with deflected and compressed magnetic fields downstream of the bow shock, strong draped and induced magnetic fields near the planet, and an extended two-lobe draped magnetotail downstream of Mars. The current sheet between the two lobes is an important channel for ion escape [*Barabash et al.*, 2007; *Fedorov et al.*, 2006; *Dubinin et al.*, 2011] and a possible site of reconnection and other dynamic processes [*DiBraccio et al.*, 2015; *Harada et al.*, 2015]. The clear organization of the draped fields in the magnetosphere by the upstream interplanetary magnetic field (IMF) demonstrates that the thorough correction of the MAG data produced accurate measurements of weak upstream IMF vectors. The turbulent fluctuations in the magnetic field also have great scientific value, since they provide an effective identification of the bow shock and magnetic pileup boundaries [*Mazelle et al.*, 2004; *Vignes et al.,* 2000]. The highest amplitude fluctuations are confined in the magnetosheath between these two boundaries (Figure 3, top left). Finally, combining MAG vectors with Solar Wind Ion Analyzer (SWIA) plasma flow velocities [*Halekas et al.*, 2013a], we derive the $\mathbf{V} \times \mathbf{B}$ convection electric field (Figure 3, top right), one of the main drivers responsible for accelerating newborn ions to escape velocity. This electric field is primarily responsible for producing an escaping "polar plume" of pickup ions on the dayside of Mars [*Dubinin et al.*, 2006; *Jakosky et al.,* 2015b; *Brain et al.*, 2015; *Curry et al.,* 2015; *Dong et al.*, 2015]. The convection electric field as illustrated in this figure is relatively insensitive to the presence of strong crustal fields near the planet's surface owing to the orbital geometry

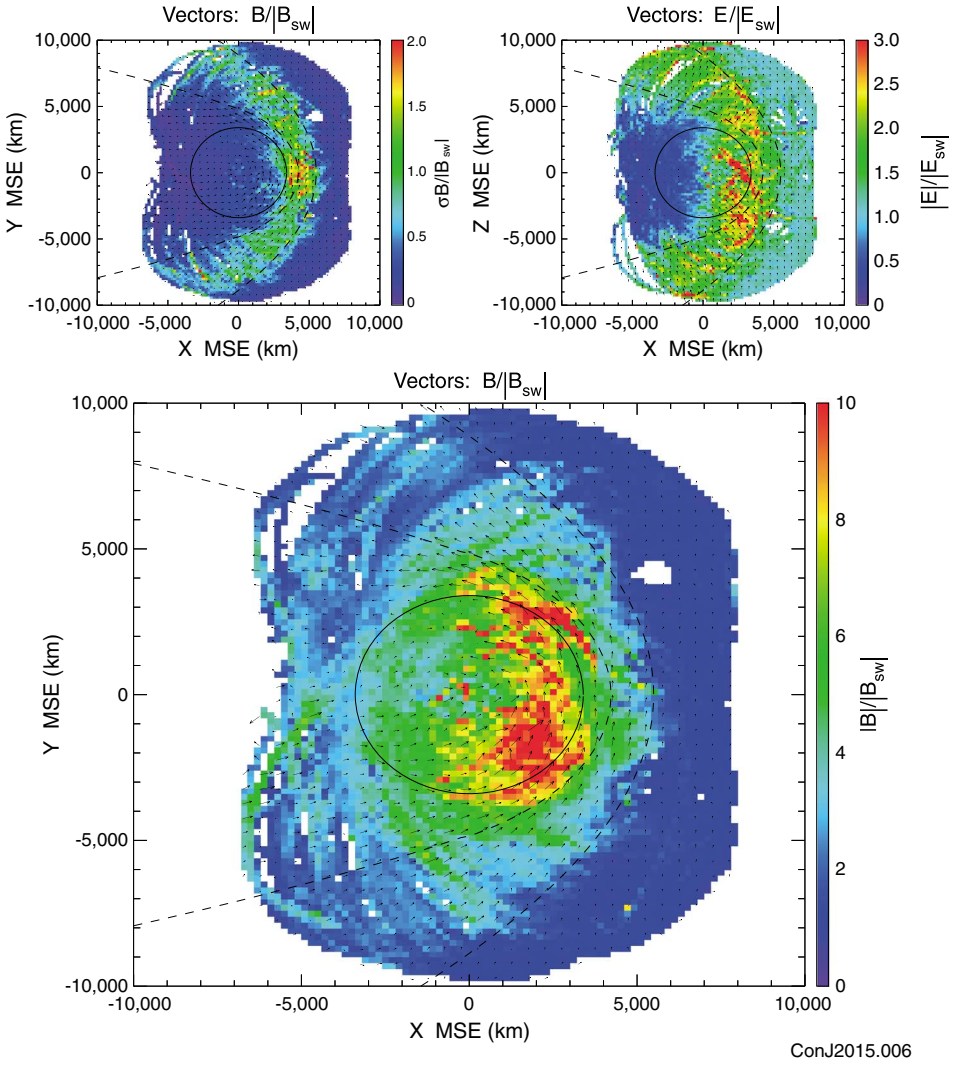

Figure 3. Statistical averages of magnetic and convection electric fields around Mars, measured during 27 November 2014 to 17 March 2015 by MAG and SWIA. All panels utilize Mars Solar Electric (MSE) coordinates: the *X* axis is antiparallel to the upstream solar wind flow measured by SWIA, and *y* is chosen to put the upstream IMF vector in the *X-Y* plane with positive *y* component. (bottom) Colors show magnetic field strength in the MSE *X-Y* plane, normalized by the orbit-averaged upstream IMF strength. Vectors show normalized field components. (top left) Colors show magnetic field Root Mean Squared (RMS) deviations over a 4 s interval in the MSE *X-Y* plane, normalized as above. (top right) Colors show convection electric field computed from SWIA's bulk flow velocity and MAG vectors projected to the MSE *X-Z* plane, normalized by the orbit-averaged upstream solar wind convection electric field. Vectors show normalized electric field components.

during this interval (northern hemisphere periapsis). The strongest convection electric fields are found predominately in the magnetosheath.

4.2. Upstream and Foreshock Waves

MAVEN's ~4.5 h orbit provides many opportunities to sample upstream solar wind. One example of upstream magnetic wave activity is presented. At ~ 7:06 UTC, DOY 361, 2014 MAG observed a series of remarkable magnetic waves (Figure 4). MAVEN was upstream of the bow shock by a few hundred kilometers, at solar zenith angle of ~60°. MAVEN's entrance into the bow shock (BS) and turbulent magnetosheath [*Espley et al.*, 2004] can be seen (Figure 4 at the right).

Strong wave activity at ~0.1 Hz is observed in all components of the magnetic field. The wavelet spectrum [*Torrence and Compo*, 1998] of B_y is shown, but the highly coherent signals at ~0.1 and ~1 Hz can also be seen

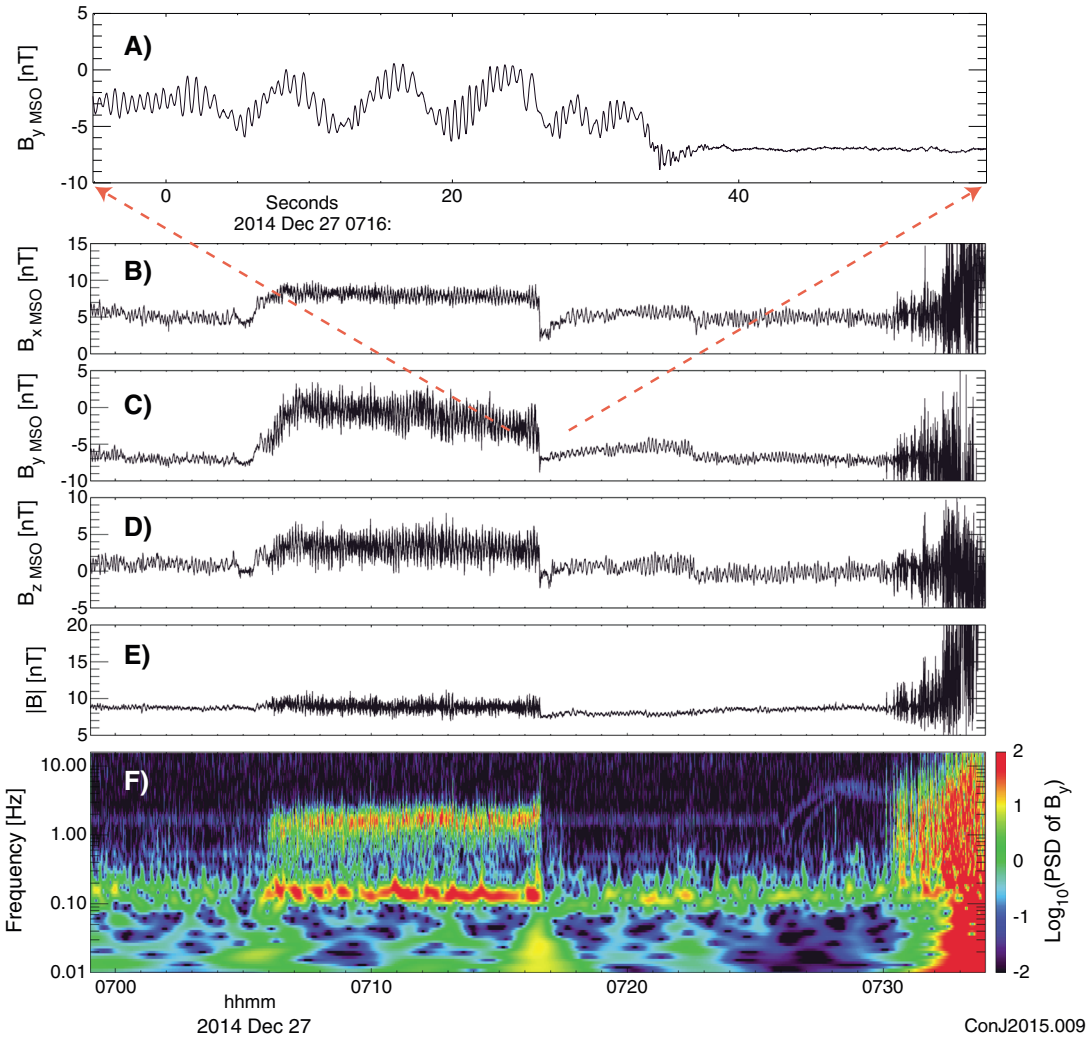

Figure 4. MAG wave events upstream of the bow shock (BS). (a) A high time resolution plot of the B_y component (Mercury Solar Orbital (MSO) coordinates) extracted from the interval indicated. (b–d) Magnetic *x*, *y*, and *z* components and (e) field magnitude are shown for 0.5 h prior to entering the Mars BS (at the right). (f) A wavelet spectrum of B_y appears. Intense "1 Hz" and ~0.1 Hz waves are seen when the interplanetary field intersects the BS (see text). The faint signature of MAVEN reaction wheels can also be seen throughout the interval at ~0.5 Hz and ~1.5 Hz, rising to ~5 Hz between ~7:27 and ~7:30.

in Figure 4a. The ~0.1 Hz frequency is as expected for proton cyclotron waves (PCWs) gyrating in the local |B| of ~9 nT. These low-frequency waves have been observed before at Mars [*Russell et al.*, 1990; *Delva and Dubinin*, 1998; *Brain et al.*, 2002; *Bertucci et al.*, 2013; *Romanelli et al.*, 2013; *Wei et al.*, 2014] and have been attributed to beam instabilities (solar wind protons reflected from BS) or pickup of ionized hydrogen from the exosphere.

Another strong signal at ~1 Hz ("1 Hz waves" hereafter) is seen from 7:06–7:17 UTC. During this interval, the PCWs persist, even stronger than elsewhere. Figure 4a shows both of the dominant wave modes and emphasizes how coherent the waves are until at 7:16:40 UTC normal solar wind behavior abruptly returns. A significant rotation in the background magnetic field occurred with the appearance and disappearance of the 1 Hz waves. Before and after the 1 Hz waves, the background magnetic field direction is quasi-parallel to the normal of the model shock [*Trotignon et al.*, 2006] whereas during the 1-Hz waves the field is quasi-perpendicular to the shock normal. A minimum variance analysis [*Song and Russell*, 1999] confirms that the 1 Hz waves are very strongly right-hand circularly polarized.

These characteristics are consistent with 1 Hz waves observed previously at Mars [*Brain et al.*, 2002] and other planets throughout the solar system [*Heppner*, 1967; *Orlowski and Russell*, 1995; *Halekas et al.*, 2013b; *Le et al.*, 2013].

The narrow range of frequencies observed (always ~1 Hz) and similar locations (upstream of a bow shock) point to a common physical mechanism that is insensitive to local solar wind conditions. They have been called upstream whistlers [*Fairfield*, 1974] but remain poorly understood.

These 1 Hz waves have amplitudes of several nanotesla; with $\Delta B/|B|$ often > 0.2, they are likely highly nonlinear. Plasma instruments usually do not have the temporal resolution to capture 1 Hz waves, but even so there appears to be an enhancement of >1 keV electrons. Similar episodes are commonly observed on adjacent orbits, but they are not as prevalent as at Mercury [*Le et al.*, 2013].

Finally, we use this set of observations to identify the faint signals at ~0.5 and ~1.5 Hz that extend across the entire interval. These signals are artifacts produced by the RWAs as discussed in section 2. Spacecraft engineering telemetry confirms that RWA #3 spun at a frequency of ~0.5 Hz until it spun up to 5 Hz at ~7:27 UTC. RWAs #1 and #2 were both operating at ~1.5 Hz until they also spun up to 5 Hz. These signals are nearly coincident with the naturally occurring 1-Hz waves, so one must take care in interpretation of magnetic spectra. The RWA speeds are available in spacecraft ancillary data, and will be archived with the MAVEN particles and fields data.

4.3. Magnetotail Dynamics

The Martian magnetotail is formed as the IMF drapes around the planet and consists of two lobes of antiparallel fields, separated by a cross-tail current sheet. Since Mars lacks a global intrinsic magnetic field, the tail orientation evolves in response to the variable IMF clock angle. *DiBraccio et al.* [2015] addresses magnetotail dynamics at Mars, providing the first clear evidence of substorm-like signatures at Mars. Observations of loading and unloading of tail magnetic flux, along with magnetic flux ropes shed during the unloading intervals (periods of decreased $|B|$), suggest a role for magnetic reconnection in tail reconfiguration.

The most distant tail measurements made by MAVEN to date (~2.6 R_M antisunward) revealed a high-energy population of planetary ions confined exclusively to the tail current sheet as they escape tailward [*DiBraccio et al.*, 2015]. These bursty plasma flows were previously identified in the Martian magnetotail using Mars Express data [*Dubinin et al.*, 2012]; however, their association with the cross-tail current sheet could not be unambiguously demonstrated prior to availability of MAVEN's simultaneous magnetic field and plasma observations. *DiBraccio et al.* [2015] observed a magnetic flux rope in association with a cross-tail current sheet traversal and suggested that magnetic reconnection events might be responsible for the tailward acceleration of these ions. Repeated tail current sheet crossings observed during a single orbit revealed a flapping or wavelike motion of the plasma sheet in response to solar wind variability.

5. Summary

The MAVEN magnetic fields investigation provides accurate vector magnetic field observations throughout science operations. Two-sensor vector measurements were used to identify spacecraft-generated magnetic fields. We conducted spacecraft maneuvers and subsystem tests to characterize "static" and dynamic spacecraft magnetic fields, now both analytically removed from measurements. Magnetic field vector accuracy was independently verified by comparison with SWEA electron distributions. In MAVEN's first few months, we have mapped the magnetospheric BS and Magnetic Pileup Boundary (MPB), and the $\mathbf{V}\times\mathbf{B}$ convection electric field and upstream wave activity, both central to atmospheric escape and MAVEN's primary science objectives.

Acknowledgments
This research was supported by a NASA Postdoctoral Program appointment (G. A. DiBraccio) at the NASA Goddard Space Flight Center, administered by Oak Ridge Associated Universities through a contract with NASA, and by the CNES for the part based on observations with the SWEA instrument embarked on Maven. We also gratefully acknowledge the support of project staff at GSFC and Lockheed Martin for contributions to the design and execution of in-flight maneuvers and subsystem tests required to characterize and mitigate spacecraft magnetic fields. Data used in this study are available at the planetary plasma interactions planetary data system node (http://ppi.pds.nasa.gov/project/maven/).

The Editor thanks two anonymous reviewers for their assistance in evaluating this paper.

References

Acuña, M. H., J. E. P. Connerney, P. Wasilewski, et al. (2001), The magnetic field of Mars: Summary of results from the aerobraking and mapping orbits, *J. Geophys. Res.*, *106*, 23,403–23,417, doi:10.1029/2000JE001404.

Barabash, S., A. Fedorov, R. Lundin, and J. A. Sauvaud (2007), Martian atmospheric erosion rates, *Science*, *315*(5811), 501–503.

Bertucci, C., et al. (2003), Magnetic field draping enhancement at the Martian magnetic pileup boundary from Mars global surveyor observations, *Geoph ys. Res. Lett. 30*(2), 1099, doi:10.1029/2002GL015713.

Bertucci, C., N. Romanelli, J. Y. Chaufray, D. Gomez, C. Mazelle, M. Delva, R. Modolo, F. González-Galindo, and D. A. Brain (2013), Temporal variability of waves at the proton cyclotron frequency upstream from Mars: Implications for Mars distant hydrogen exosphere, *Geophys. Res. Lett.*, *15*, 3809–3813, doi:10.1002/grl.50709.

Brain, D. A., Bagenal, F., Acuña, M. H., Connerney, J. E. P., Crider, D. H., Mazelle, C., Mitchell, D. L., and Ness, N. F. (2002), Observations of low-frequency electromagnetic plasma waves upstream from the Martian shock, *J. Geophys. Res.*, *107*(A6), 1076, doi:10.1029/2000JA000416.

Brain, D. A., S. Barabash, S. Bougher, F. Duru, B. Jakosky, and R. Modolo (2015), Solar wind interaction and atmospheric escape, in *The Mars Atmosphere*, edited by B. Haberle et al., Cambridge Univ. Press, Cambridge.

Connerney, J. E. P., M. H. Acuña, N. F. Ness, G. Kletetschka, D. L. Mitchell, R. P. Lin, and H. Reme (2005), Tectonic implications of Mars crustal magnetism, *Proc. Natl. Acad. Sci. U.S.A.*, *102*(42), 14,970–14,975.

Connerney, J. E. P., J. Espley, P. Lawton, S. Murphy, J. Odom, R. Oliversen, and D. Sheppard (2015), The MAVEN magnetic field investigation, *Space Sci. Rev.*, doi:10.1007/s11214-015-0169-4.

Crider, D., D. A. Brain, M. H. Acuna, D. Vignes, C. Mazelle, and C. Bertucci (2004), Mars Global Surveyor observations of solar wind magnetic field draping around Mars, *Space Sci. Rev.*, *111*(1–2), 203–221, doi:10.1023/b.spac.0000032714.66124.4e.

Curry, S. M., J. Luhmann, Y. Ma, M. Liemohn, C. Dong, and T. Hara (2015), Comaprative pick-up ion distributions at Mars and Venus: Consequences for atmospheric deposition and escape, *Planet. Space Sci.*, doi:10.1016/j.pss.2015.03.026.

Delva, M., and E. Dubinin (1998), Upstream ULF fluctuations near Mars, *J. Geophys. Res.*, *10*, 317–326, doi:10.1029/97JA02501.

DiBraccio, G. A., et al. (2015), Magnetotail dynamics at Mars: Initial MAVEN observations, *Geophys. Res. Lett.*, doi:10.1002/2015GL065248, in press.

Dong, Y. X., et al. (2015), Strong plume fluxes observed by MAVEN: An important planetary ion escape channel, *Geophys. Res. Lett.*, doi:10.1002/2015GL065346, in press.

Dubinin, E., et al. (2006), Electric fields within the Martian magnetosphere and ion extraction: ASPERA-3 observations, *Icarus*, *182*, 337–342, doi:10.1016/j.icarus.2005.05.022.

Dubinin, E., M. Fraenz, A. Fedorov, R. Lundin, N. Edberg, F. Duru, and O. Vaisberg (2011), Ion energization and escape on Mars and Venus, *Space Sci. Rev.*, *162*, 173–211, doi:10.1007/s11214-011-9831-7.

Dubinin, E., M. Fraenz, J. Woch, T. L. Zhang, J. Wei, A. Fedorov, S. Barabash, and R. Lundin (2012), Bursty escape fluxes in plasma sheets of Mars and Venus, *Geophys. Res. Lett.*, *39*, L01104, doi:10.1029/2011GL049883.

Espley, J. R., P. A. Cloutier, D. A. Brain, D. H. Crider, and M. H. Acuña (2004), Observations of low-frequency magnetic oscillations in the Martian magnetosheath, magnetic pileup region, and tail, *J. Geophys. Res.*, *109*, A07213, doi:10.1029/2003JA010193.

Fairfield, D. H. (1974), Whistler waves observed upstream from collisionless shocks, *J. Geophys. Res.*, *79*, 1368–1378, doi:10.1029/JA079i010p01368.

Fedorov, A., et al. (2006), Structure of the Martian wake, *Icarus*, *182*(2), 329–336.

Feldman, W. C., J. R. Asbridge, S. J. Bame, M. D. Montgomery, and S. P. Gary (1975), Solar wind electrons, *J. Geophys. Res.*, *80*, 4181–4196, doi:10.1029/JA080i031p04181.

Halekas, J. S., E. R. Taylor, G. Dalton, G. Johnson, D. W. Curtis, J. P. McFadden, D. L. Mitchell, R. P. Lin, and B. M. Jakosky (2013a), The solar wind ion analyzer for MAVEN, *Space Sci. Rev.*, doi:10.1007/s11214-013-0029-z.

Halekas, J. S., A. R. Poppe, J. P. McFadden, and K.-H. Glassmeier (2013b), The effects of reflected protons on the plasma environment of the moon for parallel interplanetary magnetic fields, *Geophys. Res. Lett.*, *40*, 4544–4548, doi:10.1002/grl.50892.

Harada, Y., et al. (2015), Marsward and tailward ions in the near-Mars magnetotail: MAVEN observations, *Geophys. Res. Lett.*, doi:10.1002/2015GL065005, in press.

Heppner, J. P. (1967), Recent measurements of the magnetic field in the outer magnetosphere and boundary regions, *Space Sci. Rev.*, *7*, 166–190, doi:10.1007/BF00215594.

Jakosky, B. M., et al. (2015a), The 2013 Mars Atmosphere and Volatile EvolutioN (MAVEN) mission to Mars, *Space Sci. Rev.*, doi:10.1007/S11214-015-0139-X.

Jakosky, B. M., J. M. Grebowsky, J. G. Luhmann, and D. A. Brain (2015b), Initial Results from the 397 MAVEN Mission to Mars, *Geophys. Res. Lett.*, doi:10.1002/2015GL065271, in press.

Le, G., P. J. Chi, X. Blanco-Cano, S. Boardsen, J. A. Slavin, B. J. Anderson, and H. Korth (2013), Upstream ultra-low frequency waves in Mercury's foreshock region: MESSENGER magnetic field observations, *J. Geophys. Res. Space Physics*, *118*, 2809–2823, doi:10.1002/jgra.50342.

Mazelle, C., et al. (2004), Bow shock and upstream phenomena at Mars, *Space Sci. Rev.*, *111*, 115–181, doi:10.1023/B:SPAC.0000032717.98679.d0.

Orlowski, D. S., and C. T. Russell (1995), Comparison of properties of upstream whistlers at different planets, *Adv. Space Res.*, *16*, 137–141, doi:10.1016/0273-1177(95)00220-9.

Romanelli, N., C. Bertucci, D. Gómez, C. Mazelle, and M. Delva (2013), Proton cyclotron waves upstream from Mars: Observations from Mars Global Surveyor, *Planet. Space Sci.*, *76*, 1–9, doi:10.1016/j.pss.2012.10.011.

Rosenbauer, H., R. Schwenn, E. Marsch, B. Meyer, H. Miggenrieder, M. D. Montgomery, K. H. Muhlhauser, W. Pilipp, W. Voges, and S. M. Zink (1977), A survey on initial results of the Helios plasma experiment, *J. Geophys. Res.*, *42*, 561–580.

Russell, C. T., J. G. Luhmann, K. Schwingenschuh, W. Riedler, and Y. Yeroshenko (1990), Upstream waves at Mars: Phobos observations, *Geophys. Res. Lett.*, *17*, 897–900, doi:10.1029/GL017i006p00897.

Song, P., and C. T. Russell (1999), Time series data analyses in space physics, *Space Sci. Rev.*, *87*, 387–463, doi:10.1023/A:1005035800454.

Torrence, C., and G. P. Compo (1998), A practical guide to wavelet analysis, *Bull. Am. Meteorol. Soc.*, *79*, 61–78.8, doi:10.1175/1520-0477.

Trotignon, J. G., C. Mazelle, C. Bertucci, and M. H. Acuña (2006), Martian shock and magnetic pile-up boundary positions and shapes determined from the Phobos 2 and Mars Global Surveyor data sets, *Planet. Space Sci.*, *54*, 357–369, doi:10.1016/J.Pss.2006.01.003.

Vignes, D., C. Mazelle, H. Rme, M. H. Acuña, J. E. P. Connerney, R. P. Lin, D. L. Mitchell, P. Cloutier, D. H. Crider, and N. F. Ness (2000), The solar wind interaction with Mars: Locations and shapes of the bow shock and the magnetic pile-up boundary from the observations of the MAG/ER Experiment onboard Mars Global Surveyor, *Geophys. Res. Lett.*, doi:10.1029/1999GL010703.

Wei, H. Y., M. M. Cowee, C. T. Russell, and H. K. Leinweber (2014), Ion cyclotron waves at Mars: Occurrence and wave properties, *J. Geophys. Res. Space Physics*, *119*, 5244–5258, doi:10.1002/2014JA020067.